38th AIAA/ASME/SAE/ASEE Joint Propulsion Conference & Exhibit
7-10 July 2002, Indianapolis, Indiana

AIAA 2002-4259

AIAA-2002-4259
A Numerical Study of Neutralization and Sputtering Processes in the NSTAR Thruster

Jerold W. Emhoff and Iain D. Boyd
University of Michigan
Ann Arbor, MI

38th AIAA/ASME/SAE/ASEE
Joint Propulsion Conference & Exhibit
7-10 July 2002
Indianapolis, Indiana

A NUMERICAL STUDY OF NEUTRALIZATION AND SPUTTERING PROCESSES IN THE NSTAR THRUSTER

Jerold W. Emhoff, Graduate Student Research Assistant
Iain D. Boyd, Associate Professor
Department of Aerospace Engineering
University of Michigan, Ann Arbor, MI 48109

Abstract

A computational model is used to calculate the neutralization lengths upstream and downstream of a single aperture of the optics in the NSTAR ion thruster. These data are compared to theoretical results, showing that the theoretical results are not accurate. The computed data are then analyzed to find appropriate curve fits giving the neutralization lengths for a range of operating conditions. The resulting relations compare very well to the modeled data. Molybdenum sputtered from the optics is also simulated. The amount of molybdenum depositing on the optics is calculated, as is the amount which flows upstream and downstream of the optics. It is found that nearly 25% of the sputtered material deposits on the accel grid barrel. Results are provided to illustrate the density and velocity of the sputtered molybdenum.

Introduction

The success of the Deep Space One mission and the NSTAR ion thruster have led the way to further research in the operation of ion thrusters. As such, computer simulation of ion thruster operations is more important than ever. Experiments on ion thrusters, especially life-tests, are costly and time-consuming. Computer simulations attempt to reduce both of these factors by predicting behavior for ion thrusters relatively quickly and cheaply. Ion thrusters are not simple to model, so continual improvements and modifications must be made to ensure that the best possible results are obtained. Recent advancements in ion thruster simulation include fully three-dimensional codes developed by Wang et al[1] and Nakayama and Wilbur[2]. Wang's code focuses on modeling erosion behavior in the NSTAR thruster, while the code developed by Nakayama has been applied to high specific impulse thrusters. The focus of this paper is on the improvement of a DSMC-PIC code developed to simulate ion thruster optics. This code has previously been verified to accurately model ion thrusters by Boyd and Crofton[3], and it is an excellent basis for providing further modeling of the details of ion thruster operation.

In its present state, the code assumes that the plasma flow is neutralized at both the upstream and downstream edges of the computational domain. Lengths must be chosen upstream and downstream of the optics corresponding to the neutralization lengths of the domain. If these distances are too short, then results from the simulation are unreliable. If the distances are too long, the simulation takes longer to run than necessary. The neutralization lengths are far from constant, as they vary with any change in the domain state variables such as beamlet current or discharge potential. A study is therefore undertaken to find a general relation involving some of the domain variables, so that any given simulation can be run with appropriate neutralization lengths.

Aperture widening caused by erosion of the optics is the primary mode of failure in an ion thruster. An accurate method for predicting erosion is therefore necessary to the modeling of ion thrusters. Some progress has been made in this area- the model in Ref. 1 predicts erosion on the downstream face of the accel grid very well compared to experimental data, and Ref. 2 compares very well to experimental measurement of erosion of the accel grid barrel. However, neither model has incorporated simulation of the sputtered optics material, although it has the potential to be important to the operation of the thruster. Sputtered molybdenum which flows upstream of the optics coats the walls of the discharge chamber[4], and material which flows downstream can contaminate the spacecraft. If the molybdenum deposits on the optics it is possible that the total amount of erosion is reduced, but this behavior is very difficult to detect experimentally. Simulation of sputtered molybdenum is added to the model to address these concerns.

Presented in the following is the method used to determine the neutralization lengths as a function of input beamlet current, discharge potential, and accel grid voltage. Comparisons are given between the computed data, derived relations, and theoretical results. Data is given for the density and velocity of the simulated molybdenum. Also computed are the proportions in which the molybdenum flows upstream, flows downstream, and deposits on the various parts of the optics.

Model Operation

The computational code is a 2-D axisymmetric simulation of a single aperture in an ion thruster. The grid used is composed of evenly spaced rectangular

cells. The optics of the thruster are simulated using boundary cells in the domain. These cells may be arranged in an irregular way, allowing the simulation of cusps on the barrels of the grids.

The code uses the Particle-In-Cell[5] (PIC) method to simulate xenon ions, xenon neutrals, doubly-charged xenon ions, and molybdenum. Each computational particle has a numerical weight which indicates the actual number of atoms represented by the particle. Flow field quantities for each cell are obtained by averaging the properties of all the particles in the cell, taking into account the weight of each particle. The potential field accelerates ions self-consistently. Electrons are modeled as a fluid, and the Poisson equation is solved using the Alternating Direct Implicit (ADI) method. Electron densities are retrieved from the potential using the Boltzmann relation. The Direct Simulation Monte Carlo (DSMC) method[6] is used for processing particle collisions. Both charge exchange and momentum exchange collision types are simulated. Collisions are modeled between all species except molybdenum.

To run a simulation, the optics geometry, beamlet current, and mass flow rate are first determined. These are translated into the computational geometry and the input ion and neutral densities. The simulation begins by operating at a high time-step with only neutral particles in the domain. This allows the slow moving neutrals to reach a steady state flow much more quickly. Once a steady-state is reached, ions are injected at the upstream boundary with the Bohm velocity and the input density corresponding to the desired beamlet current. At this point, the time-step is decreased so that the ions are not able to cross more than one cell boundary in a single iteration. Some fraction of the ions impact on the screen grid, reducing the output beamlet current. This fraction changes with the beamlet current, so the beamlet currents referred to below are input beamlet currents.

A typical simulation has approximately 600,000 particles. About 150,000 of these are singly charged ions and 350,000 are neutrals. There are also on the order of a few thousand doubly-charged ions. If sputtered molybdenum is being simulated, the number of such particles is approximately 100,000. For a typical domain size, about 3000 iterations are needed to initialize the neutral particle flow, followed by approximately 20,000 iterations to initialize the ion flow before sampling begins. Once a steady ion flow has been reached, data is sampled from the simulation over a large number of time-steps, typically on the order of 10,000. On a 500 Mhz Pentium III PC, a typical simulation has a running time of approximately eight hours.

Neutralization Length Study

To determine where neutralization occurs, the simulation is run with a sufficiently large domain upstream and downstream of the optics to ensure neutralization. The optics geometry for the test simulations is the standard NSTAR geometry, with cusps included on the grid barrels. Figure 1 shows the computational grid, with the white space indicating the location of the optics. For simulations requiring longer neutralization lengths, the domain length is increased accordingly. For this neutralization study, neutral particles are not introduced into the domain, and are only created by ions impacting on the optics. This greatly reduces the running time of the simulation, from 8 hours to approximately 3 hours.

The code returns output data including the densities of ions and electrons on the centerline, where the ion density is normally highest and most difficult to neutralize. Figure 2 illustrates a typical centerline electron and ion density profile. The location of the optics and the two neutralization lengths are indicated as well. This data is then analyzed to find where neutralization occurs.

The exact location of neutralization is difficult to characterize. For the upstream flow, it is the point at which centerline ion and electron densities are equal, but some amount of buffer space must be allowed in the simulation, or else the neutralization is destroyed. Downstream, the centerline ion and electron densities do not always reach equality, but instead approach each other, then remain a fairly constant distance apart, as Figure 2 shows. Some point of this near approach is decided to be the point of quasi-neutrality, but this point is somewhat arbitrary.

The shape of the computed electron density profile along the axis of an aperture is approximately the same, no matter the operating conditions, so that it simply translates in the axial direction, or increases or decreases in magnitude. This observation is used to arbitrarily set a condition to monitor. The centerline electron density at the upstream edge of the domain is taken as a reference value, $n_{e\ ref}$. Then, the distance from the upstream face of the screen grid to the point at which the centerline electron density first drops below $0.1n_{e\ ref}$ is determined, as is the length from the downstream face of the accel grid to where the centerline electron density first rises above $0.1n_{e\ ref}$. These distances are then increased by a constant amount to set the neutralization length. The value for

$n_{e\ ref}$ and the upstream and downstream $0.1n_{e\ ref}$ locations are also shown in Figure 2.

There are obvious problems with this method. Foremost is that under certain conditions, the high-density region of the beamlet diverges from the centerline, as does the critical region for downstream neutrality. This can occur with very high beamlet currents as well as with very high or very low discharge potentials. However, a beamlet with such a divergence is most likely not of practical interest, so this problem is not dealt with at this time. Computed results for beamlet currents over 1.81×10^{-5} A are excluded from the downstream neutralization length analysis because of beamlet divergence.

Another problem occurs for simulations with low beamlet currents, as the ion beam does not converge enough for the centerline electron density to rise above $0.1n_{e\ ref}$. This can also occur when the velocity of the ions is high enough such that the density remains below $0.1n_{e\ ref}$. This problem can be addressed by observing that the value of $0.1n_{e\ ref}$ is somewhat arbitrary, and a smaller value such as $0.05n_{e\ ref}$ can be used just as effectively in its place. Even though data may not be collected for simulations with this problem, any general relations still predict the correct neutralization lengths for these operating points.

This study focuses on only three of the many domain variables: input beamlet current, accel grid potential, and discharge potential. Simulations are run with three different approaches: first, with varying input beamlet current and constant discharge and accel potential; second, with varying discharge potential and constant accel potential and input beamlet current; third, with varying accel voltage and constant input beamlet current and discharge voltage. When the discharge potential is changed, the voltage drop to the screen grid is maintained at a constant 26 V. Input beamlet current is used because, as noted above, the output beamlet current is some fraction of the input beamlet current, and that fraction changes as a function of beamlet current. To keep the analysis simpler, input beamlet current is used throughout this report.

Three different types of data sets giving the length to $0.1n_{e\ ref}$ upstream and downstream of the optics are taken. The first type holds the discharge potential at a constant 1100 V and the accel grid potential at –180 V, while the input beamlet current is varied. These data are shown in Table 1. The second type varies the reference potential at a constant accel potential of –180 V. Each set of this type is simulated for a different beamlet current. Data from these sets is shown in Table 2 for the upstream length and in Table 3 for the downstream length. The third type holds the discharge potential at 1100 V while the accel potential is varied. As in the second type, each set is run for a different input beamlet current. Data for the downstream length to $0.1n_{e\ ref}$ for this set are given in Table 4. In all simulations, the electron temperature is assumed to be 5 eV upstream of the optics and 2 eV downstream of the optics.

The values to be added to the $0.1n_{e\ ref}$ lengths upstream and downstream are determined by examining the $0.1n_{e\ ref}$ lengths themselves. These lengths change with the upstream and downstream domain length until the correct neutralization length is reached, at which point they remain constant, even if the domain lengths are increased further. For the upstream side, 0.5 mm must be added to the $0.1n_{e\ ref}$ length to obtain neutralization. On the downstream side, a value of 1.5 mm is found to be necessary.

Comparison to Theoretical Results

Kaufman[7] previously gave relations for upstream and downstream neutralization lengths based on Child's Law. Kaufman assumed that the flow was one-dimensional and had zero velocity at the upstream boundary. It was also assumed that the potential had zero slope at the upstream boundary. Kaufman defines the upstream neutralization length as the distance between a plane of particle emission and the screen grid. Downstream, the neutralization length is defined by Kaufman as the distance from the accel grid to the point at which neutralization is reached.

For the upstream boundary, the following relation for neutralization length was given:

$$l_{neut} = \left[\beta \frac{\left(V_{dis} - V_{scr}\right)^{3/2} r_{scr}^2 \pi}{I_{beamlet}} \right]^{1/2} \tag{1}$$

where β is defined as:

$$\beta = \frac{4\varepsilon_0}{9} \sqrt{\frac{2e}{m}} \tag{2}$$

Here $I_{beamlet}$ is the beamlet current, r_{scr} is the radius of the screen grid aperture, V_{dis} is the discharge potential, V_{scr} is the screen grid voltage, ε_0 is the permittivity of free space, e is the electric charge, and m is the mass of the propellent gas. This equation indicates that the neutralization length increases as the beamlet current decreases, and this trend is verified by the data. However, as Figure 3 shows, the neutralization length predicted by Kaufman is an order of magnitude smaller than the computed data. The theory is also scaled such

that the 4.22×10^{-4} A point equals the simulated data. The scaled version shows that while the general trend in the data is followed, the Kaufman relation increases more quickly than the data. This indicates that the neutralization length changes with beamlet current with a power closer to zero than the inverse square root. The theory predicts no change in neutralization length when the difference between the discharge potential and the screen grid is held constant, regardless of the magnitude of the discharge potential. However, Figure 4 shows that the computed data predicts a rise in neutralization length as the discharge potential increases, while the theoretical results remain constant.

For the downstream boundary, Kaufman derived the following expression:

$$l_{neut} = \left[\beta \frac{\Delta V^{3/2} r_{accel}^2 \pi}{I_{beamlet}} \left(1 + 3R^{1/2} - 4R^{3/2} \right) \right]^{1/2} \qquad (3)$$

where ΔV is the difference between the discharge and accel potentials (V_{dis}-V_{accel}), R is the ratio $V_{dis}/\Delta V$, and r_{accel} is the radius of the accel grid aperture. Again, the dependence on beamlet current is an inverse root relation, which is very different from the simulation data, as Figure 5 shows. The general trend is the same however- as beamlet current increases, neutralization lengths decreases. The theory is again much lower in magnitude than the data, and a scaled version of the theory also fails to follow the data accurately, decreasing too slowly initially, and then dropping too much at higher beamlet currents.

Holding V_{accel} and beamlet current constant and varying V_{dis} produces data with a parabolic shape, as shown in Figure 6. The neutralization length decreases to a minimum and then increases as the discharge potential increases. The theory instead predicts an almost linear variation with discharge potential, steadily increasing with discharge potential, which clearly does not match the computed data. If the accel grid voltage is varied with constant beamlet current and discharge potential, Figure 7 shows that the computed data predicts a linear increase in neutralization length as the accel voltage decreases. The theory is again nearly linear and much lower than the data. In this case however, a scaled version of the theory comes very close to the data because of its linearity.

Overall, the theoretical relations derived by Kaufman severely under-predict the simulated neutralization length both upstream and downstream of the optics. Furthermore, these relations do not vary in the same way as the computed data. Most likely, the error in the theory stems from the assumption of one-dimensional flow. This assumption does not model the apertures properly, fixing the potential inside the apertures to the grid voltages. In reality, the potential inside either of the apertures is affected by the ion flow itself as well as the potentials upstream and downstream of the grid. This indicates that the Kaufman theory is unreliable for use as a predictor of neutralization length.

The computed results are also compared to experimental data measured by Monheiser.[8] These data were obtained by measuring the neutralization length downstream of the accel grid in a seven aperture grid set, with an accel grid aperture diameter of 5 mm. The accel grid potential had a nominal value of –500 V. These domain parameters are very different from the NSTAR thruster, so only a qualitative comparison is possible.

As seen in the computed results, the experimental data predicts a sharper increase in neutralization length with decreasing beam current than predicted by the theory. The experimental measurements taken as a function of screen grid potential are somewhat scattered, making comparison to the computed results difficult. However, the experimental data clearly show that the neutralization length increases linearly with decreasing accel grid voltage, verifying the trend seen in the computed results.

The Kaufman theory gives values of neutralization length very close in magnitude to the experimental measurements, as Ref. 8 shows. This is in direct opposition to the comparison to the computed values, which are several times higher than the theory predicts. This disparity is attributed to the fact that the experimental measurements were taken over the entire thruster, at a much larger distance than in the computer simulation. The domain in the experiments is closer to being one-dimensional at this larger distance, so that the 1-D assumption of the theory is closer to being valid. As a result, the theory gives better results.

The theory fails to approach the computed results, while the trends seen in experimental data match the trends seen in the computed results. This indicates that curve fits applied to the computed data are the best approach for obtaining general relations for the neutralization lengths for a single aperture.

Upstream Neutralization Length

For the upstream case, the accel grid potential has no significant effect, so it is ignored as a variable and the data from the third set type is not used.

First, the case where input beamlet current is varied with constant discharge potential is analyzed, and a

curve fit is applied to the data to find a general relation. As seen above, the dependence on beamlet current is weaker than an inverse root curve. It is found that a combination of a natural log and an inverse power curve best fits the data, giving the following relation for neutralization length:

$$f\left(I_{beamlet}\right) = A\ln\left(\frac{I}{I_0}\right) + B\left(I^{-1.08} - I_0^{-1.08}\right) + C \qquad (4)$$

A, *B*, and *C* are constants determined by fitting the curve to data, and I_0 is a reference beamlet current, set to 0.0754 mA. Figure 8 shows that the lengths given by this fit match the data very well.

Next, the data sets with varying discharge potential are examined. Each set produces data for the upstream side of the domain best fit by a square root relation. The coefficients of the function change with beamlet current, but the curve shape remains the same. This leads to a general relation for the neutralization length of the following form:

$$g\left(V_{dis}\right) = D\left(\sqrt{V} - \sqrt{V_0}\right) + E \qquad (5)$$

where V_0 is a reference voltage, set to 1100 V. This relation provided an excellent fit for each curve corresponding to a constant beamlet current, as Figure 9 illustrates. The change in the coefficients *D* and *E* is analyzed as a function of beamlet current, and both are found to change in the same way in which the neutralization length changes with beamlet current. In other words, the two coefficient curves are also described by (4). This indicates that a generalized relation will simply multiply the function *f(I)* with the function *g(V)*, with the proper change in coefficients such that correct values for neutralization length are given.

Following this, equations (4) and (5) are non-dimensionalized and combined to give a relation for the upstream neutralization length that is a function of beamlet current and discharge potential:

$$\frac{l_{neut}}{r_{scr}} = \frac{c_1\sqrt{\beta}}{r_{scr}}\left(f\left(I\right) + c_2\right)\left(g\left(V\right) + \frac{c_3}{\sqrt{\beta}}\right) + \frac{l_0 + c_4}{r_{scr}} \qquad (6)$$

where *f* and *g* are:

$$f\left(I\right) = \ln\left(\frac{I_0}{I}\right) + \frac{c_0}{\alpha^{1.08}}\left[\left(\frac{I_0}{I}\right)^{1.08} - 1\right] \qquad (7)$$

$$g\left(V\right) = \sqrt{\frac{V}{V_0}} - 1 \qquad (8)$$

α and β are defined as follows:

$$\alpha = \frac{I_0 r_{scr}\sqrt{\varepsilon_0 m}}{e^2} \qquad (9)$$

$$\beta = \frac{V_0 \varepsilon_0 r_{scr}}{e} \qquad (10)$$

V_0 and I_0 are again the reference voltage and beamlet current, and l_0 is the neutralization length at the reference state. The constants *c* have the following values: $c_0 = -1.226\text{x}10^{12}$, $c_1 = -2.432\text{x}10^{-8}$, $c_2 = -4.336$, $c_3 = 1.284\text{x}10^{4}$, $c_4 = -1.353\text{x}10^{-3}$. The constants c_1 and c_4 have units of meters; the others are non-dimensional. Since this relation is simply a combination of the two separate parts, Figures 8 and 9 illustrate the values given by the combined function as well.

Downstream Neutralization Length

The analysis for the downstream neutralization length considers all three data set types. As a result, the relation for the downstream neutralization length is somewhat more complicated.

The data for the case with varying discharge potential is first analyzed. As noted above, data from the sets of constant beamlet current formed parabolas, which are fit by the general relation for neutralization length:

$$f\left(V_{dis}\right) = A\left(V_{dis}^2 - V_{dis,0}^2\right) + B\left(V_{dis} - V_{dis,0}\right) + C \qquad (11)$$

Here $V_{dis,0}$ is again 1100 V. Figure 10 compares the results from this relation to the computed data. The comparison is fairly good, although there are some points at higher beamlet currents which have some error. Note that at the high beamlet current of .166 mA, discharge potentials larger than 2700 V produce beam divergence which changes the computed neutralization length. This also occurs in the .113 mA beamlet current case for a discharge potential of 600 V, and most likely occurs similarly at higher beamlet currents for sufficiently low discharge potentials.

The values of the coefficients of these parabolas are then analyzed as functions of beamlet current. The first coefficient, *A*, is found to vary with the inverse of the beamlet current. The second coefficient, *B*, varies linearly with beamlet current. Finally, *C* varies as the square of beamlet current.

Using the three different functions found above, a relation is constructed to fit data for varying beamlet current and constant accel grid and discharge potentials. However, the fit obtained is not accurate for high beamlet currents. To provide a better fit a power law function is added to the previous relation, with an optimal exponent value of 0.3. The resulting function for neutralization length as a function of beamlet current is then:

$$g(I) = D\left(I^{-1} - I_0^{-1}\right) + E\left(I - I_0\right) + F\left(I^2 - I_0^2\right) + G\left(I^{0.3} - I_0^{0.3}\right) + H \tag{12}$$

I_0 is again 0.0754 mA. Figure 11 shows that this function fits the data very well at all points. The various parts of the function are then combined with the discharge potential function to obtain a relation for neutralization length as a function of both beamlet current and discharge potential:

$$f(I, V_{dis}) = A\left(I^{-1} - I_0^{-1} + B\right)\left(V_{dis}^2 - V_{dis,0}^2 + C\right) + D\left(I - I_0 + E\right)\left(V_{dis} - V_{dis,0} + F\right) + G\left(I^2 - I_0^2\right) + H\left(I^{0.3} - I_0^{0.3}\right) + J \tag{13}$$

Note that the coefficients here are unrelated to the previous coefficients.

Finally, the variation in downstream neutralization length with accel grid potential is examined. As seen above, the neutralization length data is fit very well by a relation which varies linearly with accel potential. Figure 12 shows that there is some curvature at the higher and lower beamlet currents however. The slope and intercept of these lines varies with beamlet current in the same way as the neutralization length. This indicates that multiplying the above relation (13) by the linear variation in accel potential produces the desired generalized relation. After non-dimensionalizing, this relation is the following:

$$\frac{l_{neut}}{r_{accel}} = \frac{c_8}{r_{accel}}\left[f(I, V_{dis}) + c_9\right]\left(\frac{V_{accel}}{V_{accel,0}} + c_{10}\right) + \frac{c_{11}}{r_{accel}} \tag{14}$$

where $f(I, V_{dis})$ is:

$$f(I, V_{dis}) = c_0\left[\left(\frac{I}{I_0}\right)^{-1} + c_1\right]\left[\left(\frac{V_{dis}}{V_{dis,0}}\right)^2 + c_2\right] + c_3\left(\frac{I}{I_0} + c_4\right)\left(\frac{V_{dis}}{V_{dis,0}} + c_5\right) + c_6\left(\frac{I}{I_0}\right)^2 + c_7\left(\frac{I}{I_0}\right)^{0.3} \tag{15}$$

The constants c_i are defined as follows:

$$c_0 = \frac{4.853x10^{-6}\lambda^2}{\gamma} \tag{16}$$

$$c_1 = 2.783x10^{-13}\gamma - 1 \tag{17}$$

$$c_2 = \frac{2.234x10^{-15}}{\lambda^2} - 1 \tag{18}$$

$$c_3 = 1.694x10^{-23}\gamma\lambda \tag{19}$$

$$c_4 = \frac{-4.750x10^{12}}{\gamma} - 1 \tag{20}$$

$$c_5 = \frac{-2.305x10^{8}}{\gamma} - 1 \tag{21}$$

$$c_6 = 1.270x10^{-28}\gamma^2 \tag{22}$$

$$c_7 = 8.341x10^{-6}\gamma^{0.3} \tag{23}$$

$$c_8 = -3.236x10^{-7}\kappa \tag{24}$$

$$c_9 = -2.191x10^{-2} \tag{25}$$

$$c_{10} = \frac{-3.091x10^{6}}{\kappa} - 1 \tag{26}$$

$$c_{11} = l_0 - 9.798x10^{-4} \tag{27}$$

γ, λ, and κ are defined as:

$$\gamma = \frac{I_0 r_{accel}\sqrt{\varepsilon_0 m}}{e^2} \qquad \lambda = \frac{V_{dis,0}\varepsilon_0 r_{accel}}{e} \tag{28, 29}$$

$$\kappa = \frac{V_{accel,0}\varepsilon_0 r_{accel}}{e} \tag{30}$$

l_0 is the neutralization length when $V_{dis} = V_{dis,0}$, $I = I_0$, and $V_{accel} = V_{accel,0}$. Figures 10, 11, and 12 again compare the sampled data with the function. The computed values for the neutralization length match very well to the values given by the relation, except at the points noted above.

Sputtered Molybdenum Simulation

The modeling of the sputtered grid material, molybdenum, in the NSTAR thruster is accomplished as follows. The amount of erosion caused by a particle impacting on a grid surface is calculated considering both the energy and the angle of the particle. A linear fit to data from Weijsenfeld et al[9] is used to find the erosion as a function of energy, and the relation given by Yamamura et al[10] is used to find the erosion as a function of angle of impact. Once the amount of erosion has been determined, in terms of number of atoms eroded, several new particles representing sputtered molybdenum are created in the simulation. Each particle is given the same numerical weight, such that all of the particles together represent the total amount of eroded material. The number of particles is set large enough to obtain good statistical resolution of the behavior of the eroded material. Each particle is given the same initial location as well as a unique random thermal velocity, assuming diffuse reflection, determined by the mass of the material and the temperature of the optics. The particles are then moved through the domain as neutral particles until they reach the upstream or downstream boundary, or impact on the optics. When a molybdenum particle impacts on the optics, it is assumed to redeposit, and so is removed from the simulation after its location is recorded. Collisions are not modeled for molybdenum particles, but this should have very little effect given the expected low density of molybdenum in the simulation.

For the molybdenum simulation, the 1.76 A operating point of the NSTAR thruster is considered. The aperture modeled has a beamlet current of 0.119 mA, and a mass flow rate of 0.178 μg/s. A Xe++ fraction of 0.124 is used. It is also assumed that erosion of the accel grid cusp has taken place, while the screen grid cusp remains intact, giving the computational grid shown in Figure 13.

Contours of the resulting molybdenum number density, axial velocity and radial velocity are shown in Figures 14, 15 and 16, respectively. As Figure 14 shows, the number density of the sputtered material in the optics is on the order of $1x10^{14}$ m^{-3}, confirming that the assumption of collisionless flow for molybdenum is reasonable. The number density is highest near the accel grid barrel, because that is the originating point for most of the sputtered material. The magnitude of the axial velocity is approximately the same both upstream and downstream of the accel grid, with the particles moving slowly in the axial direction close to the accel grid with some acceleration towards the ends of the domain. The contours of radial velocity show a velocity towards the centerline for particles which are sputtered from the accel grid barrel. Also shown is a region of outward velocity towards the screen grid barrel, where particles deposit, but do not originate or reflect.

The simulation predicts single aperture accel grid erosion at the rate of $2.22x10^{-14}$ kg/s, and a deposition rate of $7.35x10^{-15}$ kg/s. The amount of molybdenum leaving the domain upstream of the optics is $3.05x10^{-15}$ kg/s, and $5.00x10^{-15}$ kg/s flows out downstream. Note that there is a remaining $6.75x10^{-15}$ kg/s which is entering the domain but is not leaving or depositing on the optics. This material is most likely flowing between the grids, and would eventually deposit on either the optics near another aperture or the wall of the thruster. About 33% of the sputtered material deposits on the optics. Approximately 14% flows upstream, while 23% flows downstream, and 30% remains in the domain.

Figure 17 shows the location for ions impacting on the accel grid, and Figure 18 shows the amounts of sputtered atoms that result from all impacts. Nearly all of the erosion and ion impingement occurs on the downstream half of the accel grid barrel, with lesser amounts on the upstream half of the barrel and the downstream face of the accel grid. Figure 19 shows that most deposition activity is also seen on the accel grid barrel, although it is now evenly spread over the entire barrel. Small amounts of deposition are found on the screen grid barrel and downstream face, but no deposition is computed on the accel grid upstream and downstream faces, or the screen grid upstream face. This is expected, as erosion only occurs on the accel grid, and the sputtered particles do not collide with any other particles. The sputtered particles have no way to impact on either side of the accel grid, or the upstream side of the screen grid.

70.6% of the molybdenum deposits on the accel barrel, 24.8% deposits on the screen grid barrel, and 4.7% deposits on the screen grid downstream face. Again, no molybdenum is found to deposit on the accel grid upstream or downstream faces, or the upstream face of the screen grid. These data show that erosion may be slowed significantly by the deposition of the sputtered material. Nearly one quarter of all sputtered material deposits onto the high erosion zone of the accel grid. However, it is not known if the deposited molybdenum has the same rate of erosion as the original grid material.

It must be noted that the above simulation predicts an accel grid current of 0.83 mA, an order of magnitude lower than the 8.6 mA accel grid current measured in the NSTAR 8200 hour wear test.[11] The same wear test measured 10.81 grams of eroded material. The total erosion over 8200 hours predicted by the simulation,

without considering redeposition, is 9.68 grams, which compares very well to the experiment. However, when the redeposited material is subtracted from the computed mass loss, the result is 6.48 grams, much lower than the experimental value. While this does not necessarily invalidate the results on the behavior of the sputtered material, it is probable that the mass flow rates of the sputtered material are larger than simulated, as is the number density in the domain. Also, it is assumed that the molybdenum has a 100% chance of depositing on any surface it comes in contact with, but it is unknown how valid this assumption is.

Conclusions

Simulated data for the upstream and downstream neutralization lengths of a single aperture in the NSTAR ion thruster were generated. Theoretical results were found to be unable to predict the neutralization lengths, so curve fits to the computed data were used to find general relations for the neutralization lengths.

It was found that the dependence of the upstream neutralization length on the input beamlet current is a combination of the natural logarithm of the beamlet current and a power law with an exponent of –1.08. The upstream length also depends on the square root of the discharge potential. These two dependences were combined to obtain a general relation for the upstream neutralization length. This relation returns results which compare very well to the simulated data.

The downstream neutralization length has a parabolic shape as a function of discharge potential, and the change in the coefficients of the parabola with beamlet current led to a relation for neutralization length as a function of input beamlet current and discharge potential. The downstream length was also found to vary linearly with the accel grid voltage. This was combined with the first relation to obtain a general relation for the downstream neutralization length as a function of input beamlet current, discharge potential, and accel grid voltage. This relation compares well to most of the data, although at higher beamlet currents it is less accurate.

Modeling of sputtered molybdenum was introduced into the computational code and a simulation was performed to obtain results for the behavior of the sputtered material. The molybdenum was found to deposit only on the accel grid barrel, the screen grid barrel, and the downstream face of the screen grid. A third of the sputtered material deposits on the optics, 30% does not leave the domain, 14% flows upstream of the optics and 23% flows downstream. 70% of the total deposited material deposits on the accel grid barrel, so that 23% of the total eroded material returns to the accel grid. This may reduce erosion on the accel grid by a similar factor.

Acknowledgement

This work was funded in part by the NASA Glenn Research Center under grant NAG3-2497 with George Soulas as the technical monitor.

References

[1] Wang, J., Polk, J., Brophy, J., Katz, I., "3-D Particle Simulations of NSTAR Ion Optics," IEPC Paper 01-085, October 2001.

[2] Nakayama, Y., Wilbur, P. J., "Numerical Simulation of High Specific Impulse Thruster Optics," IEPC Paper 01-099, October 2001.

[3] Boyd, I. D., Crofton, M. W., "Grid Erosion Analysis of the T5 Ion Thruster," AIAA Paper 2001-3781, July 2001.

[4] Sovey, J. S., Dever, J. A., Power, J. L., "Retention of Sputtered Molybdenum on Ion Engine Discharge Chamber Surfaces," IEPC Paper 01-086, October 2001.

[5] Birdsall, C. K. and Langdon, A. B., *Plasma Physics Via Computer Simulation*, Adam Hilger Press, 1991.

[6] Bird, G. A., *Molecular Gas Dynamics and the Direct Simulation of Gas Flows*, Oxford University Press, 1994.

[7] Kaufman, H. R., "One-Dimensional Analysis of Ion Rockets," NASA Technical Note D-261, March 1960.

[8] Monheiser, J. M., "Development and Verification of a Model to Predict Impingement Currents for Ion Thrusters," NASA CR – 195322, April 1994.

[9] Weijsenfeld, C. H., Hoogendoorn, A., and Koedam, M., "Sputtering of Polycrystalline Metals by Inert Gas Ions of Low Energy (100-1000eV)," *Physica*, Vol. 27, 1961, p. 763.

[10] Yamamura, Y., Itikawa, Y. and Itoh, N., "Angular Dependence of Sputtering Yields of Monoatomic Solids," Report IPPJ-AM-26, Institute of Plasma Physics, Nagoya University, Japan, 1983.

[11] Polk, J. E., Anderson, J. R., Brophy, J. R., Rawlin, V. K., Patterson, M. J., Sovey, J., Hamley, J., "An Overview of the Results from an 8200 Hour Wear Test of the NSTAR Ion Thruster," AIAA Paper 99-2446, July 1999.

Table 1. Computed data for the upstream and downstream distances in millimeters from the optics to $0.1n_{e\ ref}$, as a function of input beamlet current only.

Beamlet Current (A)	Upstream Length (mm)	Downstream Length (mm)
0.2	1.495	
0.3	1.212	
0.4	1.047	
0.5	0.934	
0.6	0.852	
0.7	0.787	
0.8	0.736	1.904
0.9	0.694	1.611
1	0.657	1.426
1.1	0.622	1.289
1.2	0.596	1.199
1.3	0.567	1.127
1.4	0.546	1.077
1.5	0.521	1.042
1.6	0.504	1.009
1.7	0.483	0.983
1.8	0.466	0.964
1.9	0.453	0.952

Beamlet Current (A)	Upstream Length (mm)	Downstream Length (mm)
2	0.435	0.935
2.1	0.420	0.924
2.2	0.408	0.917
2.4	0.381	0.907
2.5	0.369	0.912
2.6	0.359	0.918
3	0.318	0.989
3.5	0.273	1.169
3.7	0.260	
4	0.237	
4.5	0.207	
5	0.173	
5.1	0.168	
5.2	0.163	
5.3	0.160	
5.4	0.156	
5.5	0.152	
5.6	0.147	

Table 2. Computed data for the upstream distance in millimeters from the optics to $0.1n_{e\ ref}$, as a function of input beamlet current and discharge potential.

	Beamlet Current (A)								
Discharge Potential (V)	6.03E-05	6.79E-05	7.54E-05	9.05E-05	9.80E-05	1.13E-04	1.36E-04	1.51E-04	1.66E-04
400	0.390								
500	0.455	0.418							
600	0.511		0.442	0.387	0.364	0.321		0.241	
700	0.562	0.524	0.491			0.369			
800	0.610		0.536	0.479		0.412			
900	0.655	0.613	0.577		0.497	0.454	0.400		
1000	0.698		0.618	0.558		0.488		0.405	
1100	0.736	0.694	0.657	0.596	0.567	0.521	0.466	0.435	0.408
1200	0.775		0.692	0.626	0.603	0.557			
1300		0.765	0.725			0.586	0.526		
1400			0.760	0.693		0.615		0.521	
1500		0.833	0.792		0.694	0.645			0.519
1600			0.822	0.754		0.670			
1700							0.634		
1800				0.808	0.775			0.622	
1900									0.614
2100						0.798	0.726		
2200								0.711	
2300									0.700
2500							0.811		
2700									0.772
3100									0.845
3500									0.912

Table 3. Computed data for the downstream distance in millimeters from the optics to $0.1n_{e\ ref}$, as a function of input beamlet current and discharge potential.

	Beamlet Current (A)								
Discharge Potential (V)	6.03E-05	6.79E-05	7.54E-05	9.05E-05	9.80E-05	1.13E-04	1.36E-04	1.51E-04	1.66E-04
400	1.918								
500	1.765	1.698							
600	1.695		1.554	1.491	1.506	1.585			
700	1.661	1.549	1.474			1.343			
800	1.669		1.422	1.311		1.228			
900	1.726	1.520	1.397		1.211	1.153	1.104		
1000	1.777		1.385	1.215		1.088		1.006	
1100	1.904	1.611	1.426	1.199	1.127	1.042	0.964	0.935	0.917
1200	2.050		1.490	1.192	1.111	1.005			
1300		1.847	1.582			0.975	0.867		
1400			1.698	1.257		0.960		0.779	
1500		2.116	1.822		1.157	0.958			0.702
1600			1.958	1.401		0.963			
1700							0.762		
1800				1.600	1.363			0.661	
1900									0.565
2100						1.213	0.785		
2200								0.619	
2300									0.472
2500							0.978		
2700									0.472
3100									0.742
3500									1.000

Table 4. Computed data for the downstream distance in millimeters from the optics to $0.1n_{e\ ref}$, as a function of input beamlet current and accel grid voltage.

	Beamlet Current (A)							
Accel Grid Voltage (V)	6.03E-05	6.79E-05	7.54E-05	8.29E-05	9.80E-05	1.13E-04	1.36E-04	1.51E-04
-140	1.336	1.147	1.026	0.952	0.851	0.786	0.732	0.712
-150	1.487	1.257	1.120	1.033	0.921	0.855	0.801	0.770
-160	1.641	1.374	1.222	1.116	0.991	0.916	0.855	0.831
-170	1.758	1.493	1.321	1.205	1.059	0.978	0.911	0.885
-180	1.904	1.611	1.426	1.289	1.127	1.042	0.964	0.935
-190	2.037	1.733	1.538	1.378	1.200	1.100	1.015	0.983

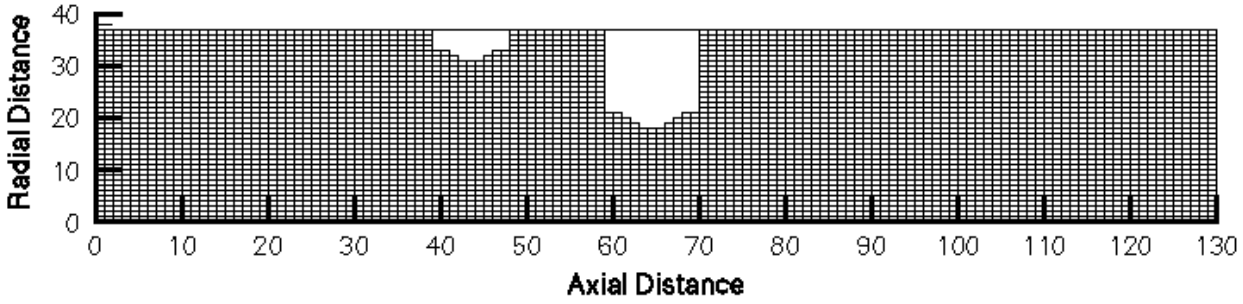

Figure 1. The computational grid used for the neutralization study. The white areas represent the optics in the simulation.

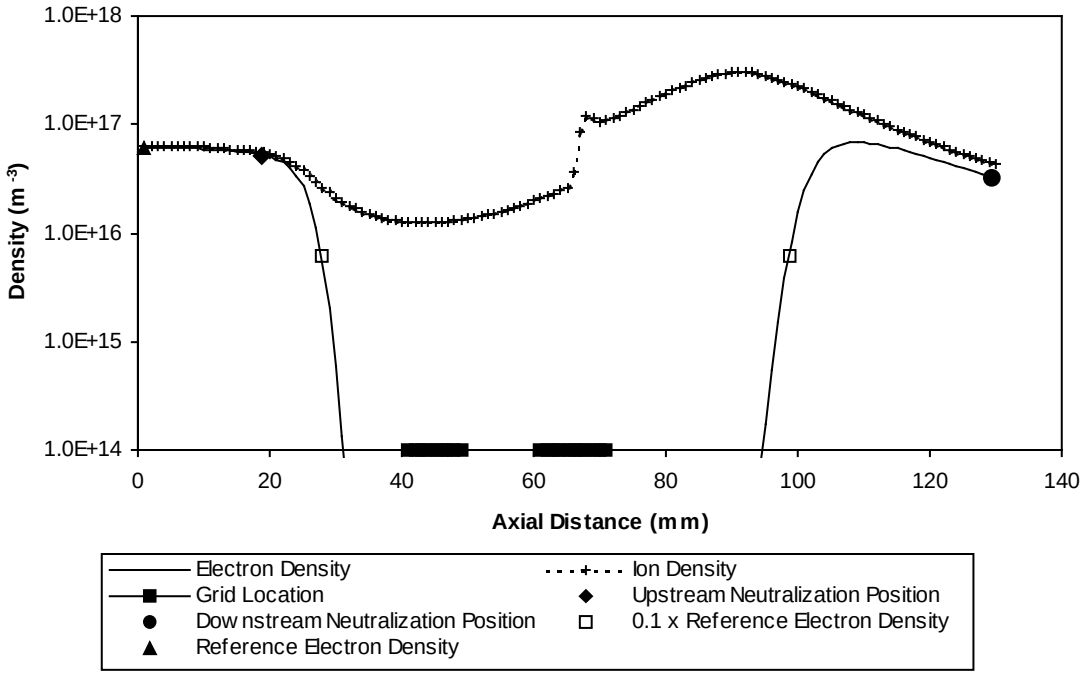

Figure 2. A typical logarithmic profile of centerline ion and electron densities. The case shown is for an input beamlet current of 7.54×10^{-5} A, 1100 V discharge potential, and –180 V accel grid voltage. The location of the grids, the reference electron density, the $0.1 n_{e\ ref}$ positions, and the neutralization positions are also shown.

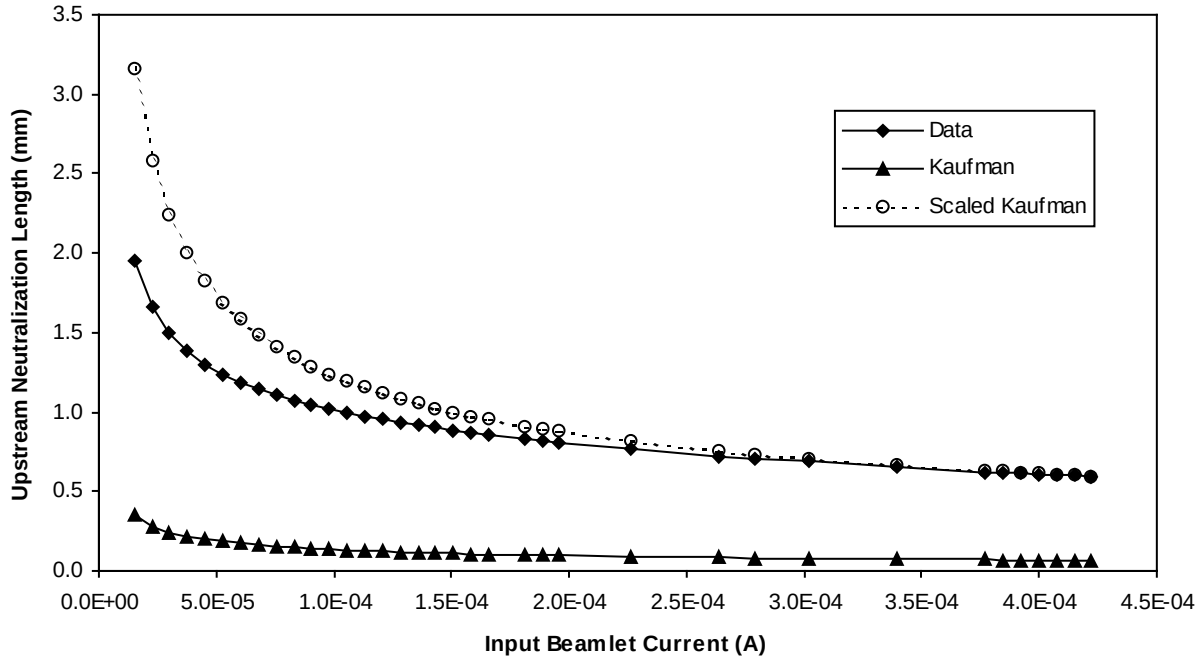

Figure 3. Comparison of the computed upstream neutralization length to the Kaufman theory as a function of input beamlet current. Also shown is the Kaufman theory scaled to equal the 1.51×10^{-5} A data point. The discharge potential is 1100 V and the accel grid voltage is –180 V for all points.

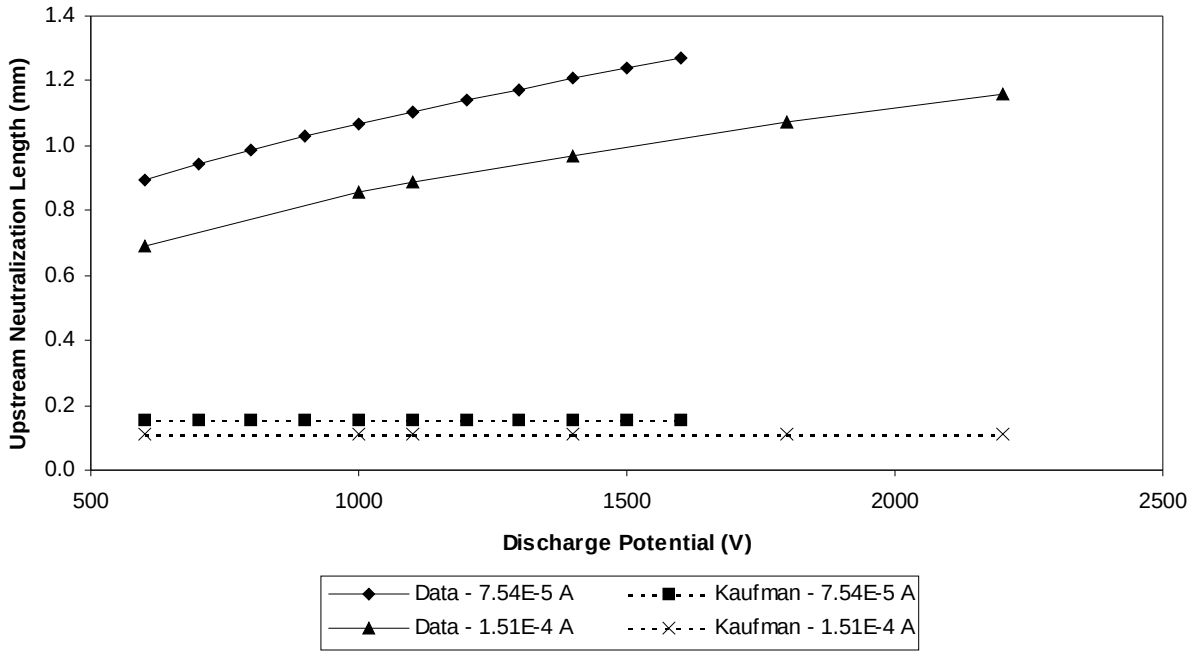

Figure 4. Comparison of the computed upstream neutralization length to the Kaufman theory as a function of discharge voltage. The accel grid voltage is –180 V for all points.

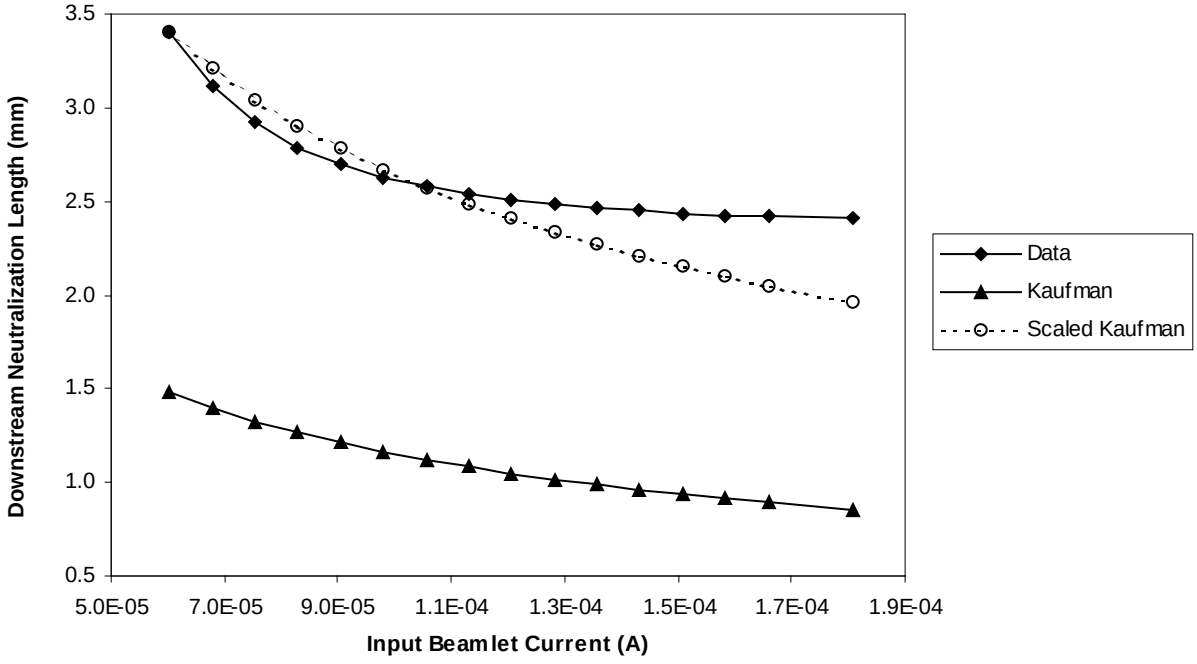

Figure 5. Comparison of the computed downstream neutralization length to the Kaufman theory as a function of input beamlet current. The Kaufman theory scaled to equal the 6.03×10^{-5} A data point is shown as well. The discharge potential is 1100 V and the accel grid voltage is –180 V for all points.

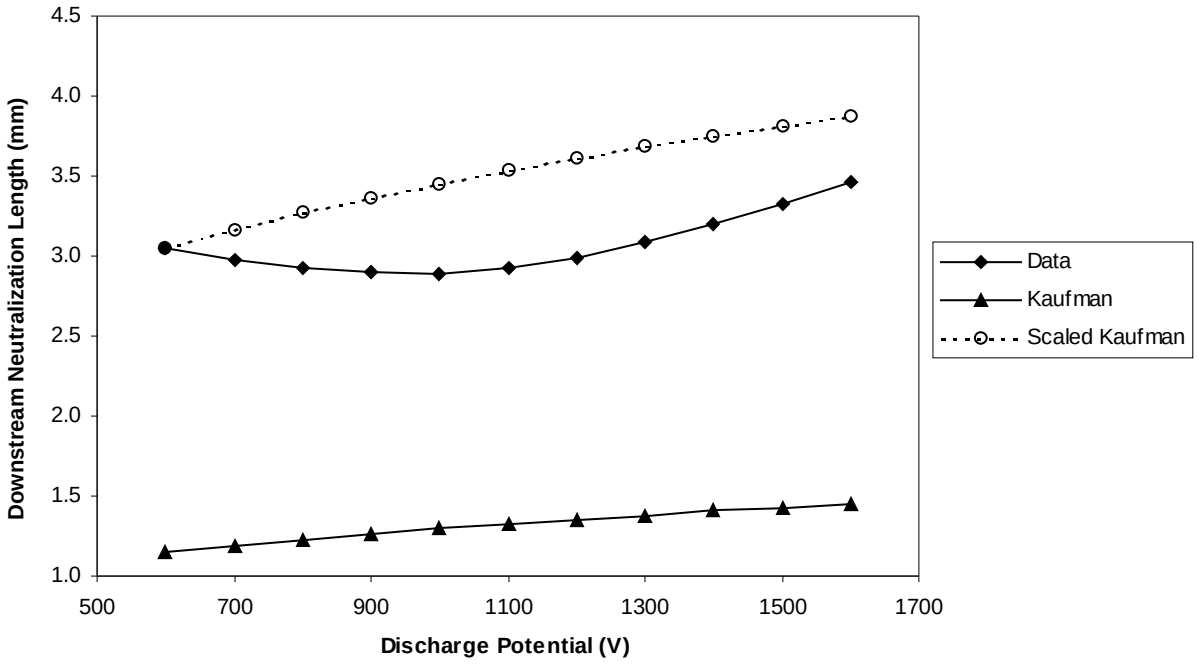

Figure 6. Comparison of the computed downstream neutralization length to the Kaufman theory and the scaled Kaufman theory as a function of discharge potential. The Kaufman theory is scaled to equal the 600 V data point. The input beamlet current is 7.54×10^{-5} A and the accel grid voltage is –180 V for all points.

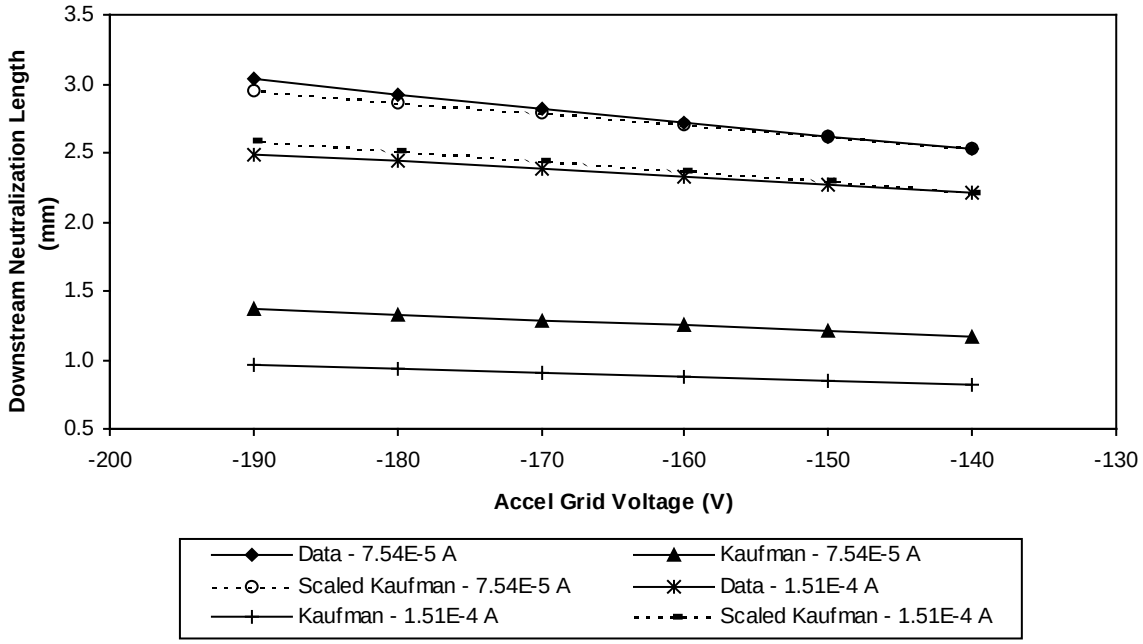

Figure 7. Comparison of the computed downstream neutralization length to the Kaufman theory and the scaled Kaufman theory as a function of accel grid voltage and input beamlet current. The Kaufman theory is scaled to equal the -140 V data point for both beamlet currents. The discharge potential is 1100 V for all points.

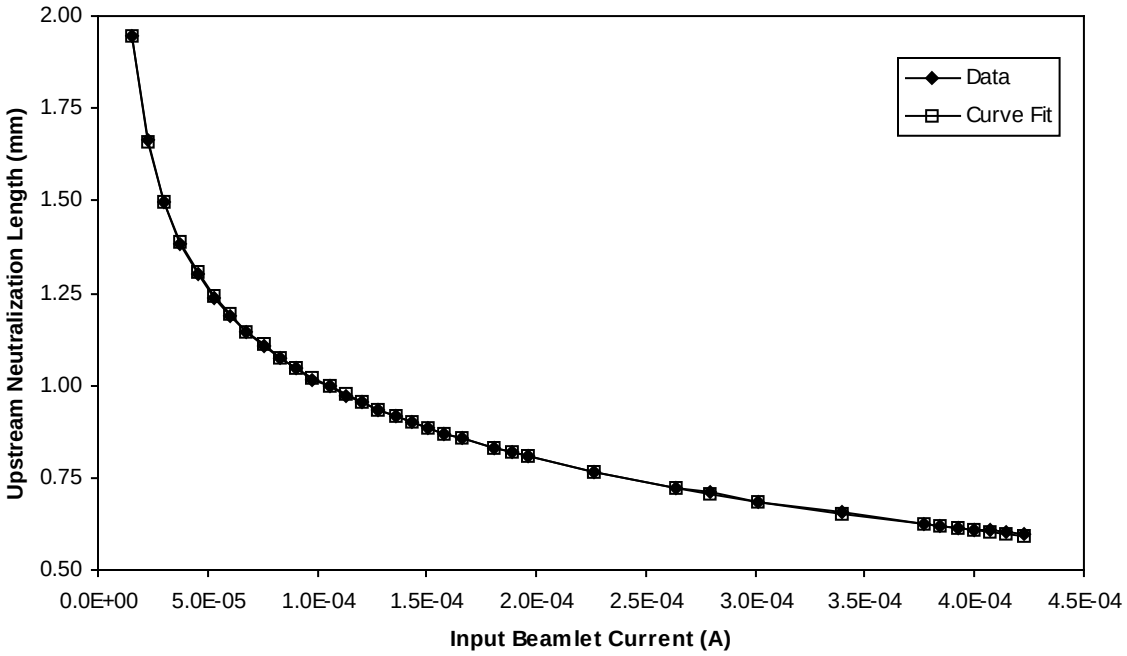

Figure 8. Comparison of the computed upstream neutralization length to the curve fit, as a function of input beamlet current. The discharge potential is 1100 V and the accel grid voltage is –180 V for all points.

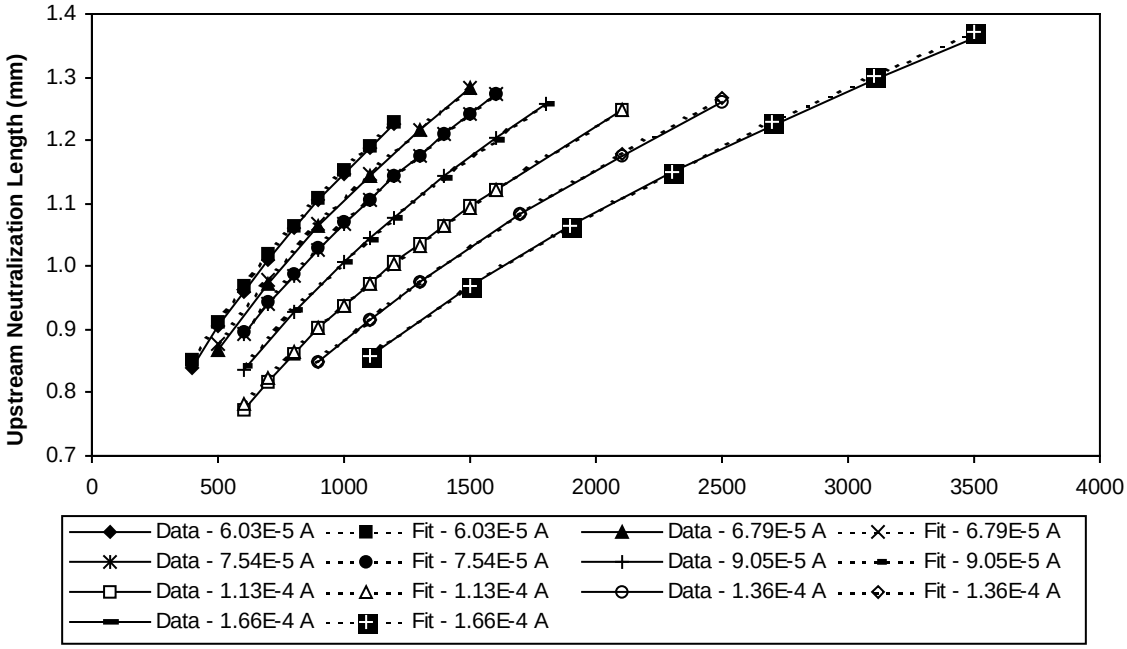

Figure 9. Comparison of the computed upstream neutralization length to the curve fit, as a function of discharge potential and input beamlet current. The accel grid voltage is –180 V for all points.

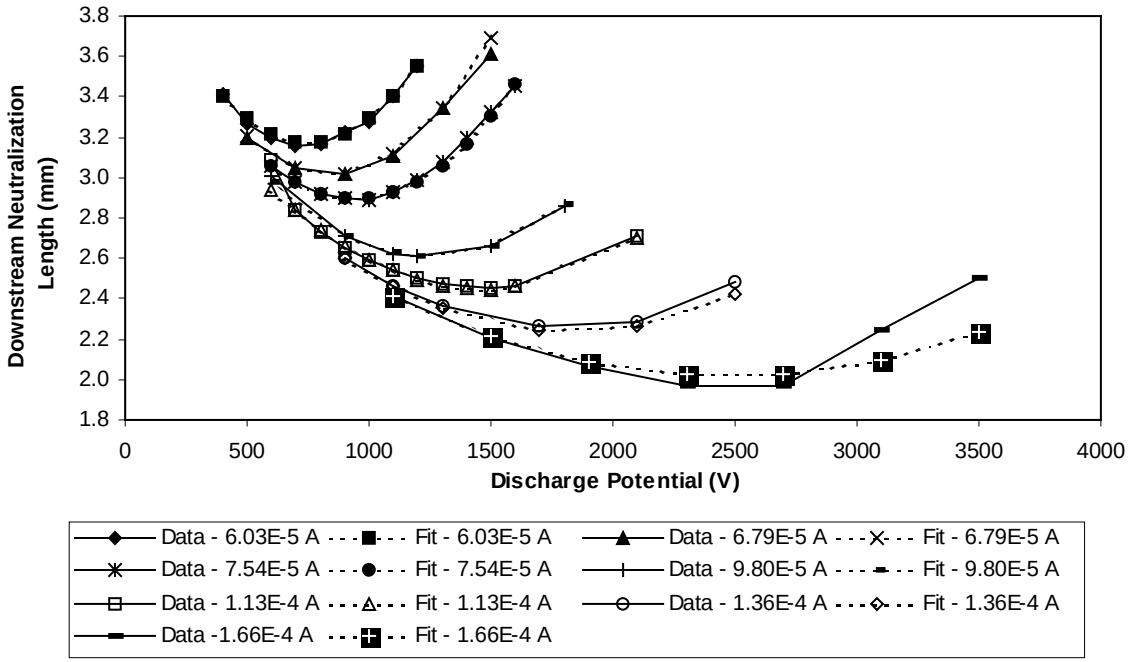

Figure 10. Comparison of the computed downstream neutralization length to the curve fit, as a function of discharge potential and input beamlet current. The accel grid voltage is –180 V for all points.

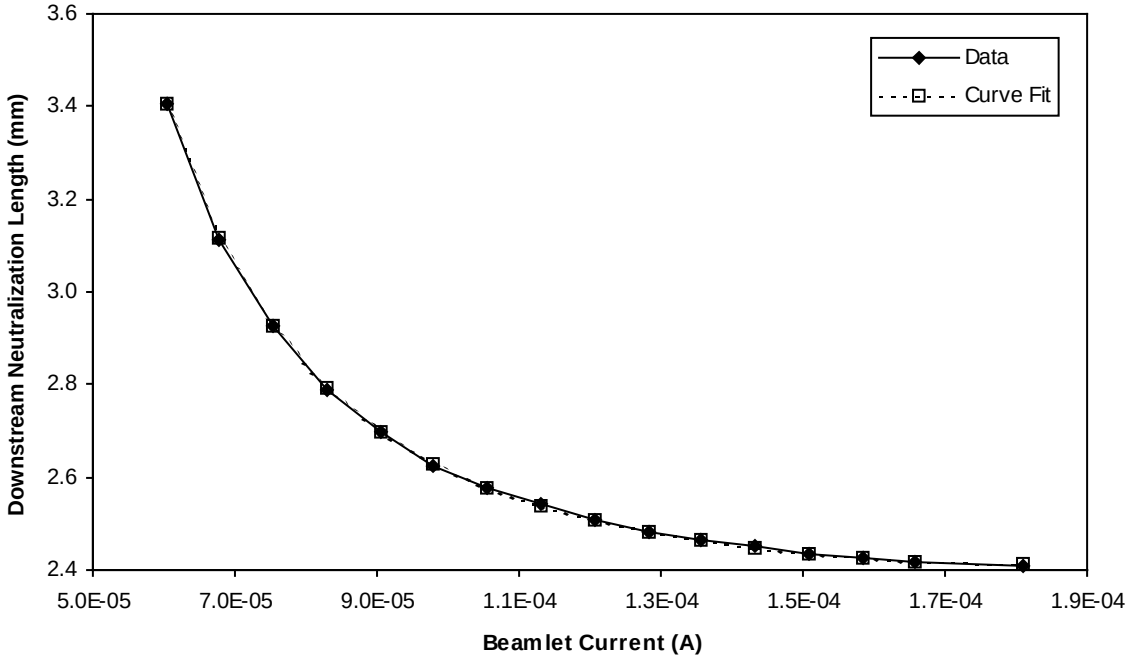

Figure 11. Comparison of the computed downstream neutralization length to the curve fit, as a function of input beamlet current. The discharge potential is 1100 V and the accel grid voltage is –180 V for all points.

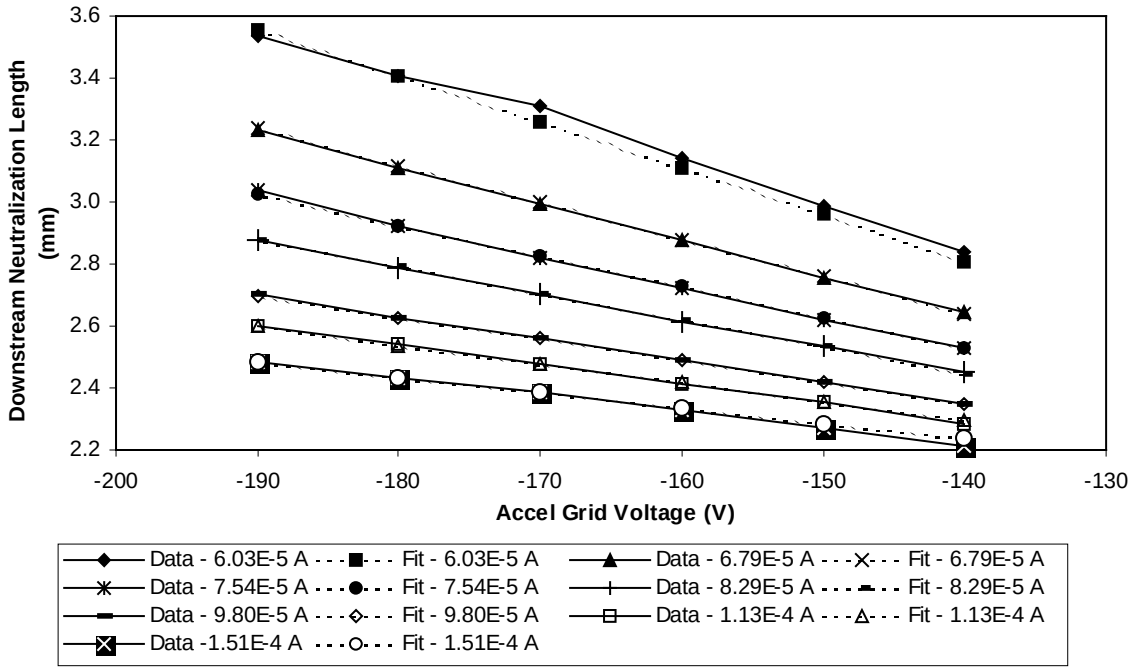

Figure 12. Comparison of the computed downstream neutralization length to the curve fit, as a function of accel grid voltage and input beamlet current. The discharge potential is 1100 V for all points.

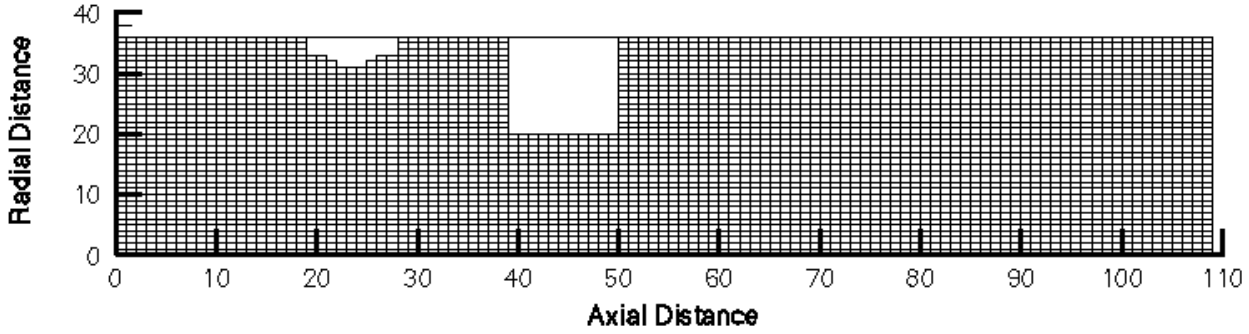

Figure 13. The computational grid used for the molybdenum simulation. The white areas represent the optics in the simulation.

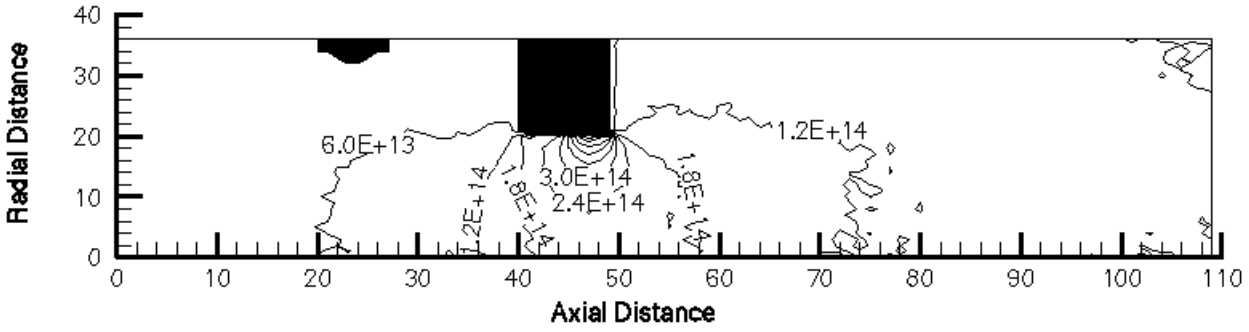

Figure 14. Contours of density for sputtered molybdenum. Values are in m^{-3}, and the black areas represent the optics.

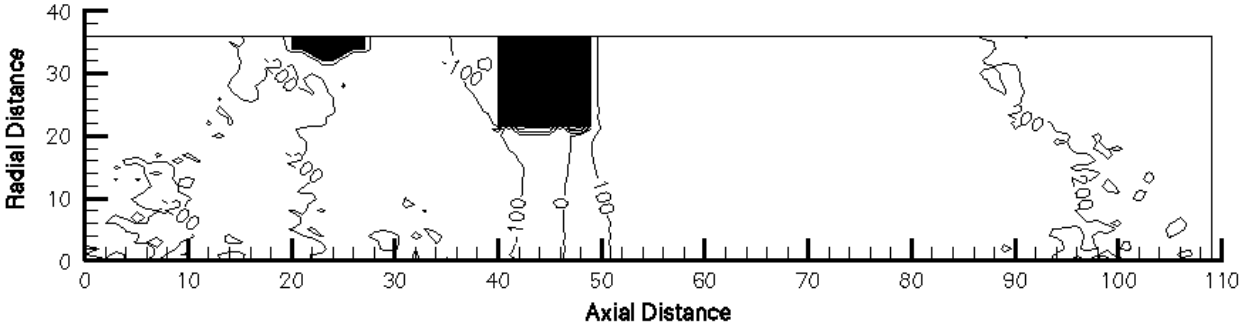

Figure 15. Contours of axial velocity for sputtered molybdenum. Values are in m/s.

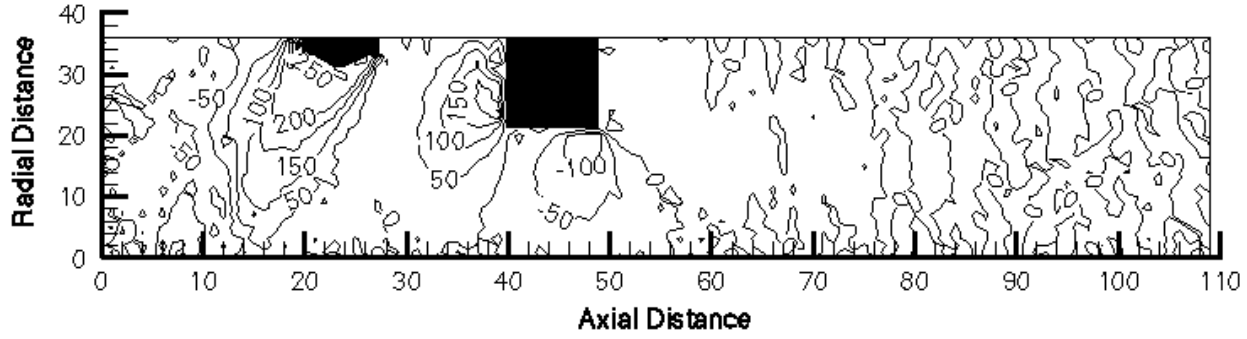

Figure 16. Contours of radial velocity for sputtered molybdenum. Values are in m/s, with positive values directed away from the centerline.

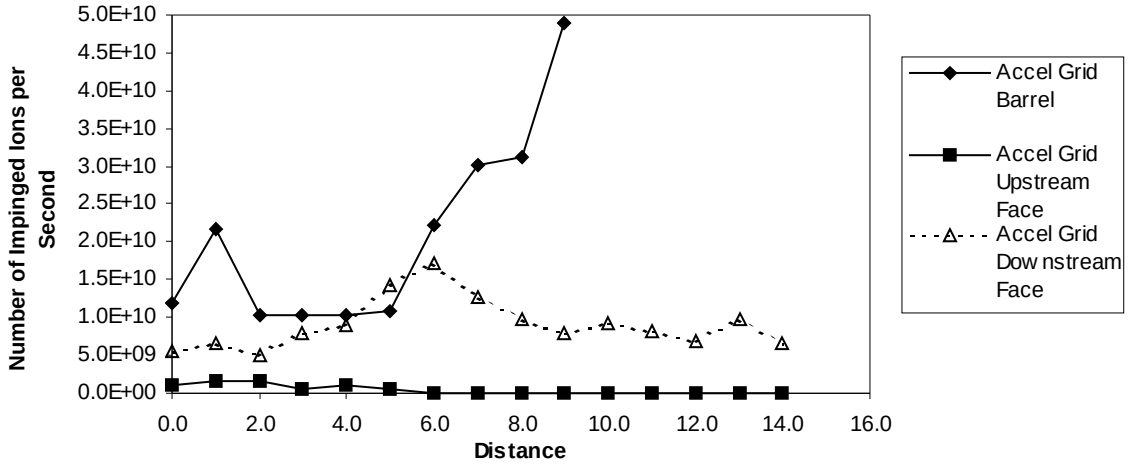

Figure 17. Plot of the number of impinged ions per second on the accel grid. The distances for the upstream face and barrel are referenced to the upstream edge of the grid, and the distances for the downstream face are referenced to the downstream edge of the grid.

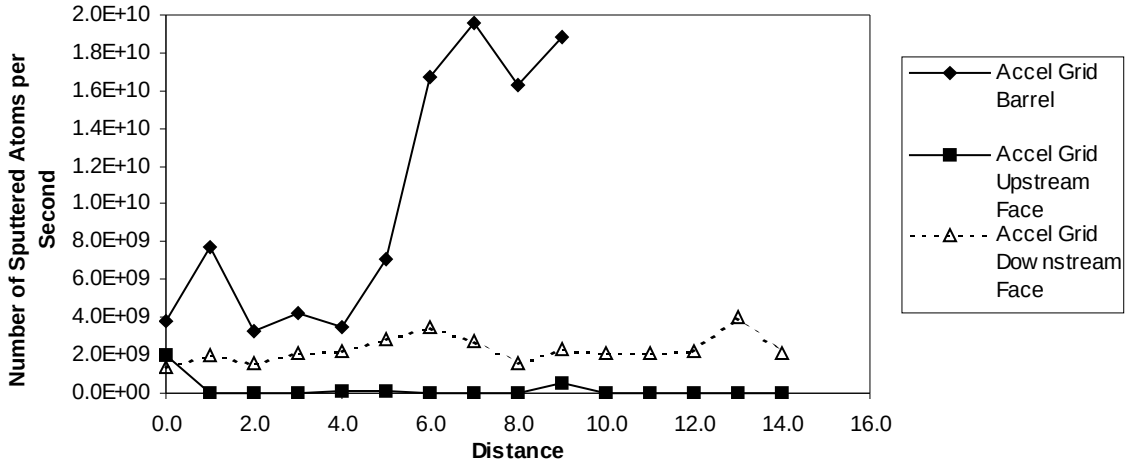

Figure 18. Plot of the number of atoms sputtered from the accel grid per second. The distances for the upstream face and barrel are referenced to the upstream edge of the grid, and the distances for the downstream face are referenced to the downstream edge of the grid.

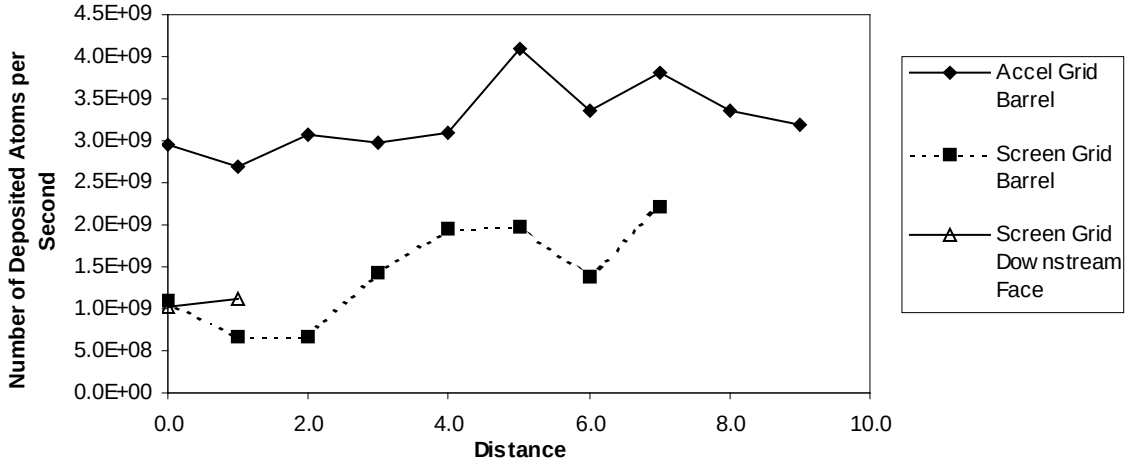

Figure 19. Plot of the number of atoms deposited on the screen and accel grids per second. The distances for the barrel of the screen grid are referenced to the upstream edge of the grid, the distances for the downstream face of the screen grid are referenced to the downstream edge of the grid, and the distances for the barrel of the accel grid are referenced to the upstream edge of the grid.